

Chinese Pharmaceutical Association
Institute of Materia Medica, Chinese Academy of Medical Sciences

Acta Pharmaceutica Sinica B

www.elsevier.com/locate/apsb www.sciencedirect.com



ORIGINAL ARTICLE

Ultrasmall, elementary and highly translational nanoparticle X-ray contrast media from amphiphilic iodinated statistical copolymers



Lu Su^{a,b,†}, Kellie S. Dalby^{a,†}, Hannah Luehmann^{c,†}, Sussana A. Elkassih^a, Sangho Cho^a, Xun He^a, Lisa Detering^c, Yen-Nan Lin^a, Nari Kang^a, Dennis A. Moore^d, Richard Laforest^c, Guorong Sun^{a,*}, Yongjian Liu^{c,*}, Karen L. Wooley^{a,*}

Received 21 July 2022; received in revised form 18 August 2022; accepted 5 September 2022

KEY WORDS

Amphiphilic statistical iodocopolymer;
CT;
X-ray contrast media;
Ultrasmall nanoassembly;
PET/CT;
Longitudinal tumor monitoring

Abstract To expand the single-dose duration over which noninvasive clinical and preclinical cancer imaging can be conducted with high sensitivity, and well-defined spatial and temporal resolutions, a facile strategy to prepare ultrasmall nanoparticulate X-ray contrast media (nano-XRCM) as dual-modality imaging agents for positron emission tomography (PET) and computed tomography (CT) has been established. Synthesized from controlled copolymerization of triiodobenzoyl ethyl acrylate and oligo(ethylene oxide) acrylate monomers, the amphiphilic statistical iodocopolymers (ICPs) could directly dissolve in water to afford thermodynamically stable solutions with high aqueous iodine concentrations (>140 mg iodine/mL water) and comparable viscosities to conventional small molecule XRCM. The formation of ultrasmall iodinated nanoparticles with hydrodynamic diameters of *ca.* 10 nm in water was confirmed by dynamic and static light scattering techniques. In a breast cancer mouse model, *in vivo* biodistribution studies revealed that the ⁶⁴Cu-chelator-functionalized iodinated nano-XRCM exhibited extended blood residency and higher tumor accumulation compared to typical small molecule imaging agents. PET/CT imaging

Peer review under the responsibility of Chinese Pharmaceutical Association and Institute of Materia Medica, Chinese Academy of Medical Sciences.

^aDepartment of Chemistry, Department of Materials Science and Engineering, and Department of Chemical Engineering, Texas A&M University, College Station, TX 77842, USA

^bLaboratory of Macromolecular and Organic Chemistry and Institute for Complex Molecular Systems, Eindhoven University of Technology, Eindhoven, MB 5600, The Netherlands

^cMallinckrodt Institute of Radiology, Washington University School of Medicine, Saint Louis, MO 63110, USA ^dBayer AG, Creve Coeur, MO 63167, USA

^{*}Corresponding author.

E-mail addresses: guorong.sun@chem.tamu.edu (Guorong Sun), yongjianliu@wustl.edu (Yongjian Liu), wooley@chem.tamu.edu (Karen L. Wooley).

[†]These authors made equal contributions to this work.

of tumor over 3 days showed good correlation between PET and CT signals, while CT imaging allowed continuous observation of tumor retention even after 10 days post-injection, enabling longitudinal monitoring of tumor retention for imaging or potentially therapeutic effect after a single administration of nano-XRCM.

© 2023 Chinese Pharmaceutical Association and Institute of Materia Medica, Chinese Academy of Medical Sciences. Production and hosting by Elsevier B.V. This is an open access article under the CC BY-NC-ND license (http://creativecommons.org/licenses/by-nc-nd/4.0/).

1. Introduction

X-ray computed tomography (CT) is a widely used imaging modality in clinics and for preclinical research with high spatial resolution^{1,2}. To enhance the CT contrast for accurate diagnosis, X-ray contrast media (XRCM) are extensively used in CT examinations³⁻⁵, which account for $\sim 40\%$ of the overall clinical CT scans carried out each year worldwide⁵. However, current contrastenhanced CT imaging suffers from narrow acquisition time windows, i.e., typically within 30 min after intravenous administration of conventional XRCM, due to rapid renal clearance of small molecule X-ray attenuated or radiopaque compounds. To broaden the operational time, gold and other high K-edge metal-based nanoparticles^{6,7}, as well as nanoparticulate XRCMs (nano-XRCMs) from iodinated liposomes⁸, nanosuspensions⁹ and nano-emulsions¹⁰, and (co)polymers^{11–19}, have been developed. Such systems have demonstrated efficiencies for differentiating vasculatures and tissues up to week(s) after initial intravenous administration^{3-7,20}. Moreover, there is often interest to enhance the imaging sensitivity, for instance by employing positron emission tomography (PET)²¹⁻²⁴, which has led to the increased development of imaging agents for dual modality PET/CT imaging^{25,26}.

Metallic nanoparticles (NPs) have shown greater capabilities for contrast-enhanced CT imaging in tumor diagnosis and treatment monitoring²⁷. To increase the biocompatibility of metallic NPs for potential translation, one of the most widely-used strategies is to reduce the particle size to ultrasmall scale^{28,29}, namely <6 nm by intensity-weighted hydrodynamic radius (R_h) , to facilitate renal clearance. Ultrasmall-sized gold NPs have exhibited advantages over iodinated small molecule XRCMs on improving cancer CT imaging quality while maintaining sufficient clearance capability^{30–32}. Ultrasmall gold NPs have also shown potential toward advancing PET/CT imaging with targeting of tumor specific biomarkers³³. While there are debates regarding the *in vivo* integrity of polymer-coated gold NPs³⁴ and the long-term toxicity concerns of transition metal and metal oxide NPs^{35,36}, ultrasmall polymeric nano-XRCMs derived from iodinated (co)polymers comprising components with well-established biocompatibilities and minimal toxicities are anticipated to enable "smoother" translations from preclinical studies to clinical research. To date, iodinated polymer nano-XRCMs from nanosuspension and nanoemulsion 13 as well as amphiphilic block copolymer nanoassembly 11,12,17 approaches have encountered challenges in realizing ultrasmall sizes. While iodinated dendrimers^{37–39} represent promising macromolecular ultrasmall nano-XRCMs, their relatively sophisticated syntheses inhibit further translation. Therefore, the development of iodinated polymer-based ultrasmall nano-XRCMs requires further innovation to achieve materials that coincidently fulfill the important criteria of high aqueous solubility and low solution viscosity at physiological temperature (37 °C); complete biocompatibility; long blood residence time; specific biodistribution through either passive or active pathways; convenient metabolism; facile access to dual-modality imaging towards improving diagnostic sensitivity; less dependency to CT specification; feasible and cost-controlled preparation.

Advances in controlled polymerization methodologies⁴⁰⁻⁴² enable systematic and precise tunings over the composition, microstructure, sequence, and topology of polymers, which are important attributes to their supramolecular assemblies in the design of polymer-based imaging agents with improved aqueous solubilities, elevated blood retention, and optimal in vivo pharmacokinetics and biodistribution. It was hypothesized that an amphiphilic statistical iodocopolymer (ICP) would provide non-biased sequence distribution of hydrophilic monomers and hydrophobic iodinated monomers within its primary linear polymer chain structure and lead to higher order assemblies, to mimic the overall globular amphiphilicity of commercially-available small molecule iodinated XRCMs, e.g., ioversol, and achieve enhancements of iodinated polymer concentrations, viscosities and dimensionalities (Fig. 1). Amphiphilic statistical copolymers tend to undergo intra/intermolecular self-assembly into NPs with relatively small hydrodynamic sizes, as confirmed by amphiphilic polymethacrylate 43,44 and polvacrylate^{45,46} copolymers consisting of statistically-arranged hydrophilic oligo(ethylene glycol) monomethyl ether and hydrophobic alkyl pendant groups. Therefore, a hydrophobic iodinated monomer, triiodobenzoyloxy ethyl acrylate (TIBEA), was designed, synthesized (Supporting Information Scheme S1A and Fig. S1), and subsequently copolymerized with hydrophilic oligo(ethylene glycol) monomethyl ether acrylate (OEGMEA) to afford a series of amphiphilic statistical ICPs (Scheme 1A) with varied degrees of polymerization (DP_n s). After assessing the water solubilities and solution-state viscosities of the series of ICPs, we comprehensively investigated the hydrodynamic radii of ICPfabricated nano-XRCMs in water, which revealed relationships between the sizes of assembled NPs and the DP_n of ICP precursors. applying a 2,2',2",2"'-(1,4,7,10-tetraazacyclododecane-1,4,7,10-tetrayl)tetraacetic acid functionalized chain transfer agent (DOTA-CTA, Scheme S1B and Supporting Information Figs. S2-S3), a DOTA-ICP with optimal composition was then synthesized (Scheme 1B) and evaluated for in vivo pharmacokinetics and PET/CT imaging in an EMT6 breast cancer mouse model.

2. Results

Linear P(OEGMEA-co-TIBEA) ICPs with statistical distribution of comonomers were synthesized by reversible addition-fragmentation chain transfer (RAFT) copolymerizations⁴⁷. Hydrophilic and nonionic monomer OEGMEA was chosen to ensure biocompatibility and antibiofouling behavior⁴⁸, as well as to avoid high osmolality,

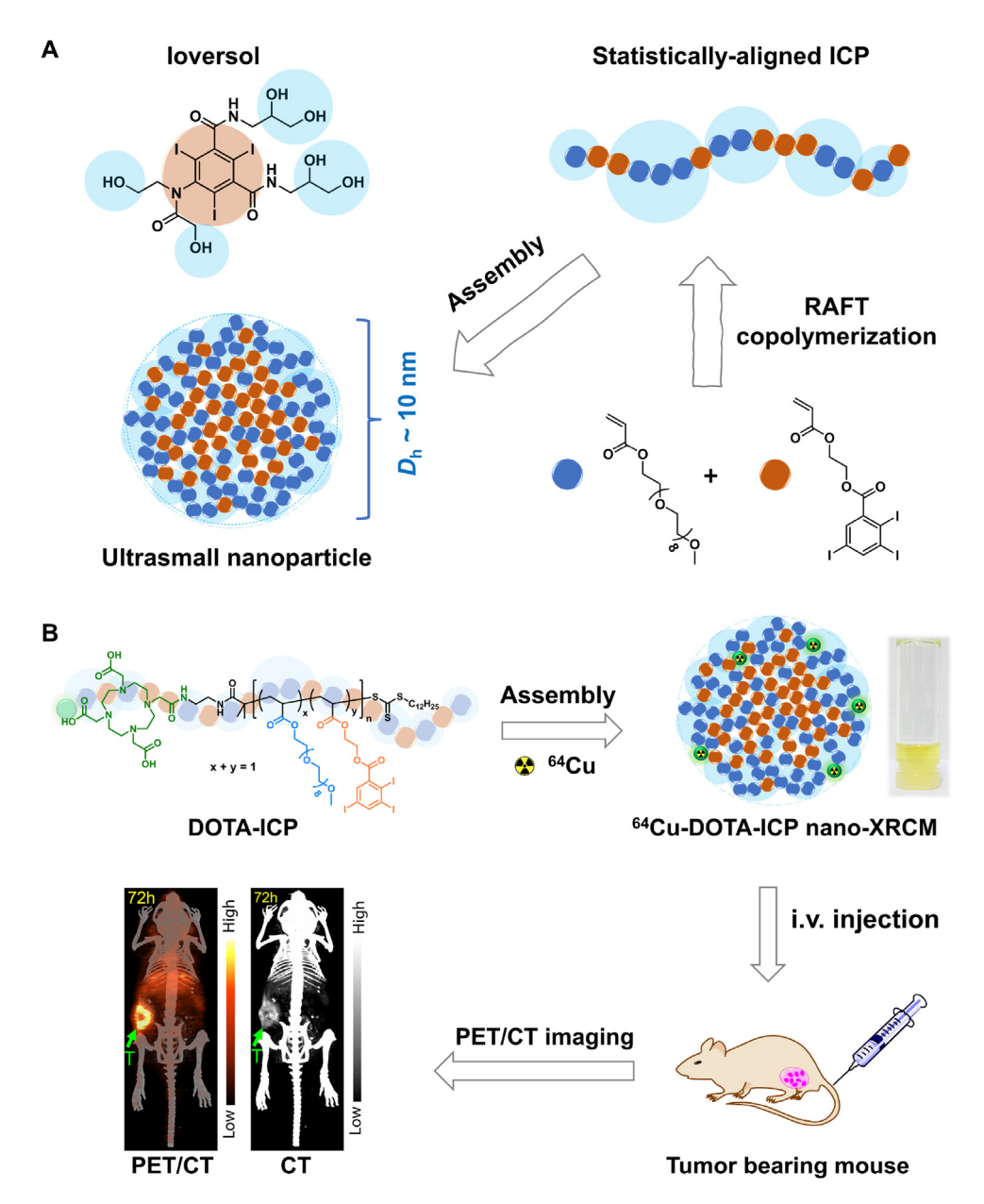
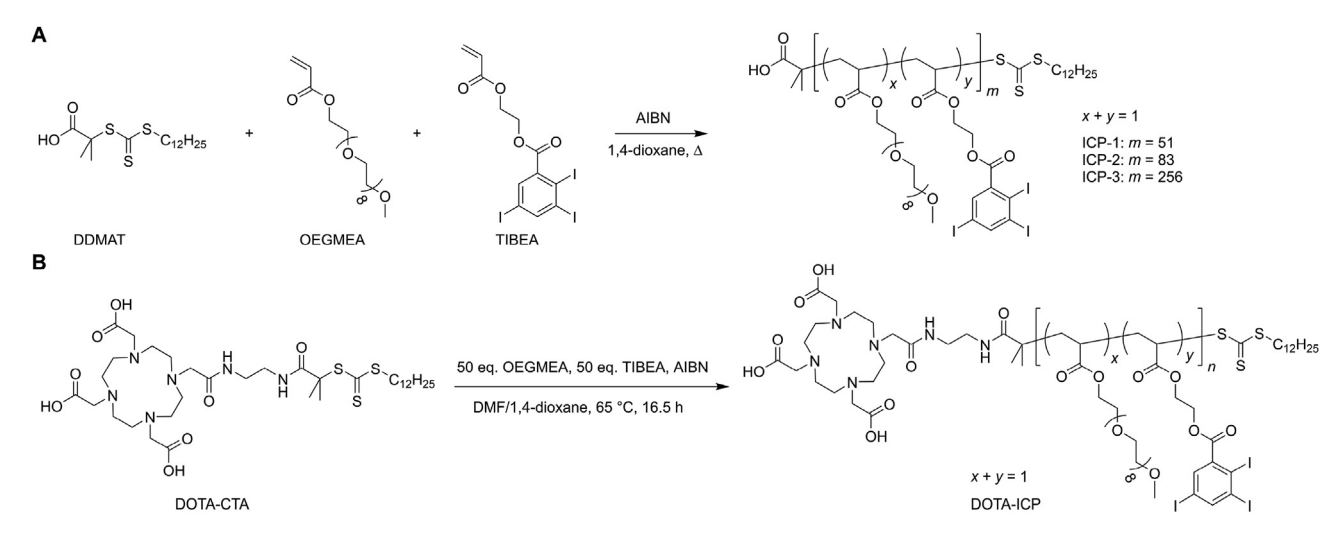


Figure 1 Schematic diagram for (A) the design of ICP, the formation and (B) applications of nano-XRCM. The inserted pictures include a vial containing a solution of DOTA-ICP (400 mg polymer/mL H₂O) (middle right), PET/CT and CT (lower left) imaging of mice bearing EMT6 breast cancer tumor at 72 h post-injection, respectively.

which is of concern for clinical ionic contrast agents. The hydrophobic monomer TIBEA was designed based upon the literature-reported methacrylate counterpart ^{13,14}. The selection of polyacrylate over polymethacrylate scaffold was based upon two aspects: i) at identical molar mass and comonomer ratio, the theoretical iodine content (I wt%) in polyacrylate is higher than that in polymethacrylate; ii) the relatively-lower glass transition temperature of polyacrylate can provide better flexibility, which is beneficial for the cross-backbone assembly of pendants ^{45,46}. RAFT polymerization was selected as this controlled radical polymerization methodology provides tolerance to the aromatic iodine moiety in TIBEA. The comonomer feed ratio was fixed as 1:1 to provide sufficient I wt% and balance the ratio of hydrophilicity/hydrophobicity in the resulting ICPs.

The OEGMEA and TIBEA monomers showed comparable conversions up to >90% (Supporting Information Table S1),

making the generation of ICPs feasible, with reliable control over the ratio between hydrophilic and hydrophobic functionalities. As summarized in Table 1, all ICPs showed satisfactory on-target compositions (x/y, 0.95-0.98), verified by ¹H NMR spectroscopy (Supporting Information Fig. S4). The size exclusion chromatography (SEC, Supporting Information Fig. S5) analyses indicated that, for ICPs with low (ICP-1) and medium (ICP-2) DP_n s, relatively-narrow molar mass distributions were achieved with dispersity (D) values of 1.2. For ICP-3, the polymerization proceeded more slowly and was, therefore, taken only to ca. 55% conversion. Nonetheless, the relatively-larger D (1.4), the asymmetric SEC profile, and the noticeable variation between the number-average molar mass by SEC using tetrahydrofuran (THF, $M_{\rm n,\ THF-SEC}$) and the theoretical $M_{\rm n}$ (Table S1) suggested a less controlled polymerization and the occurrence of unanticipated biradical coupling during the RAFT copolymerization targeting



Scheme 1 Synthetic schemes of ICPs (A) and DOTA-ICP (B) used in this study, respectively.

the higher DP_n . The I wt% of all ICPs, calculated from x/y and DP_n values and $M_{n. THF-SEC}$, was ~ 35 wt%.

The lack of block segmental arrangements of OEGMEA and TIBEA within ICP frameworks was supported by differential scanning calorimetry (DSC) assessment of the glass (T_g) and melting $(T_{\rm m})$ transition temperatures of the ICPs, in comparison to the homopolymer and block copolymer controls, i.e., POEG-MEA₇₄, PTIBEA₄₂, and POEGMEA₇₄-b-PTIBEA₄₁ (Supporting Information Scheme S2), respectively (Supporting Information Fig. S6). POEGMEA₇₄ displayed a T_g at -67 °C and a T_m at -2 °C, while PTIBEA₄₂ showed a T_g at ca. 65 °C. POEGMEA₇₄b-PTIBEA₄₁ showed two $T_{\rm g}$ s at -60 and 62 °C, revealing microphase separation within the block copolymer. By comparison, all ICPs exhibited a single $T_{\rm g}$ (-33, -32, and -35 °C for ICP-1, ICP-2, and ICP-3, respectively) without any melting endotherms, indicating the absence of long segments of POEGMEA and PTIBEA. Moreover, the rather low T_g of ICP indicated its flexibility at room temperature, which was anticipated to promote the aqueous assembly to ultrasmall sizes.

The water solubilities and solution viscosities of the ICPs were then investigated. All ICPs showed high water solubility of >500 mg ICP/mL H₂O by directly dissolving polymers into Milli-Q (MQ, 18.2 M Ω cm) water, followed by stirring at room temperature for 12 h to form clear homogeneous ICP solutions, which were thermodynamically stable over a long-term (>6 months) at

Table 1 Summary of ICPs and DOTA-ICP prepared from RAFT copolymerizations of OEGMEA and TIBEA.

1					
Polymer	x/y ^a	M _n , THF-SEC	Đ	I wt%	H ₂ O solubility
		(kDa)			(mg ICP/mL
					H ₂ O)
ICP-1	0.97	28.2	1.2	35.1	>500
ICP-2	0.98	45.2	1.2	35.4	815
ICP-3	0.98	138.5	1.4	35.5	715
DOTA-ICP	0.95	67.0	1.3	35.8	>600

^aBy ¹H NMR spectroscopy.

room temperature. Herein, statistical "delocalization" of hydrophobicity throughout the amphiphilic macromolecular framework exhibited superiority on enhancing copolymer water solubility over the block "agglomerate" counterpart, as the opaque 20 mg/ mL POEGMEA₇₄-b-PTIBEA₄₁ control was only maintained as a suspension for a few hours (Supporting Information Fig. S7). A theoretical iodine concentration of 296 mg I/mL H₂O that is similar to ioversol (300 mg I/mL H₂O) could be achieved by dissolving 820 mg of ICP-2 in 1 mL of MQ water. However, the viscosity measurements of this solution at both 23 and 37 °C showed high kinematic viscosities that were over 8 cSt (the maximum range of Cannon 25 A519 viscometer). Upon diluting the solution to 400 mg ICP-2/mL H₂O (ca. 140 mg I/mL H₂O), the kinematic viscosity value at 37 °C was found to be 4.75 cSt, which is comparable with ioversol (5.50 cSt at 37 $^{\circ}$ C). As the \sim 140 mg I/mL H₂O iodine concentration was confirmed as satisfactorily high for our system (vide infra), we did not further optimize the viscosity of the ICP solutions.

The solution behaviors of all ICPs and the block copolymer control were explored in detail through dynamic/static light scattering (DLS/SLS) techniques. As shown in Fig. 2A (also see Supporting Information Fig. S8), the R_h of the three ICPs in water was each ca. 5 nm, whereas the R_h distributions in N_hN -dimethylformamide (DMF) gradually increased with DP_n , with values centered at 2 nm (ICP-1), to 3 nm (ICP-2), and to 5 nm (ICP-3). As a note, a second distribution of NPs (~10% by intensity, $R_{\rm h} \approx 70$ nm) was observed for ICP-3 in MQ water. This larger size distribution species could be attributed to the increased D of ICP-3 compared with ICP-1 and ICP-2. The absolute weightaverage molar mass (Mw) of each ICP was evaluated by SLS in both water and good organic solvents (DMF, THF, chloroform, Fig. 2B and Supporting Information Fig. S9). The calculated $M_{\rm w}$. _{SLS} values of the ICPs in DMF were in good agreement with the $M_{\rm n,\ DMF-SEC}$ values (Table S1), suggesting the ICPs existed as single chains in DMF. As a result, the aggregation number (N_{agg}) in MQ water could be calculated by $[N_{\text{agg}} = M_{\text{w, SLS water}}/M_{\text{w,}}]$ SLS DMF], which resulted in 11.3, 4.6, and 2.4 for ICP-1, ICP-2, and ICP-3, respectively. In other words, all ICPs underwent intramolecular folding and intermolecular self-assembly to form NPs with the same R_h that was independent of DP_n . These highly regulated NP dimensions were triggered by hydrophobic

^bBy THF-SEC using light scattering detection (based on injected mass).

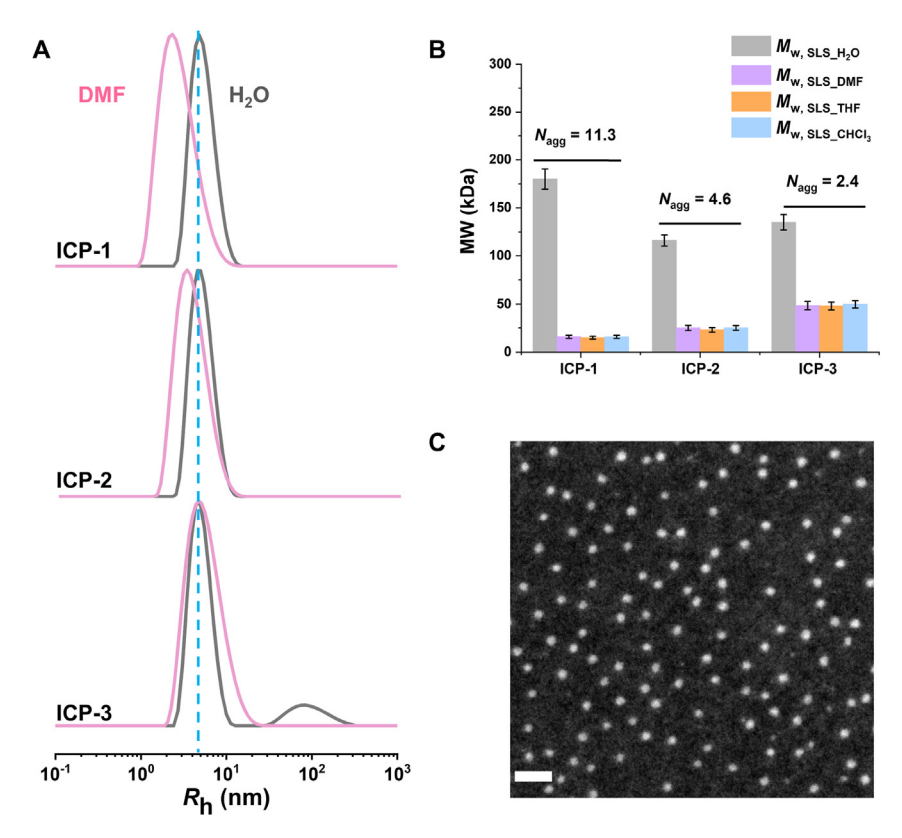


Figure 2 Characterization data of amphiphilic statistical ICPs (A) Intensity-weighted hydrodynamic radius distributions by DLS in both DMF and MQ-water with the concentration of ICP at 20 mg/mL, respectively. (B) Molar masses and aggregation numbers characterized by SLS (C) Representative STEM image of ICP solution in water (~100 mg ICP/mL H₂O). Scale bar: 50 nm.

interactions and mediated by the amphiphilicities, each provided by contributions from the polymer backbones, triiodobenzoyloxy pendants and oligoethylene glycol methyl ether side chains, as confirmed by ^1H NMR spectroscopy studies in D $_2\text{O}$, for which the proton signals disappeared for the hydrophobic components and became broadened for the OEGME protons (Fig. S4 middle). Scanning transmission electron microscopy (STEM) and TEM imaging confirmed circular shapes of these NPs with dry-state averaged radii of 5.5 \pm 1.0 nm (STEM, Fig. 2C) and 8.5 \pm 1.5 nm (TEM, Supporting Information Fig. S10), respectively, which was comparable to the observations by DLS. In sharp contrast, the amphiphilic block copolymer, POEGMEA₇₄-b-PTI-BEA₄₁, formed single chain coils in DMF ($R_h = 4$ nm) but rather large nanostructures ($R_h = 23$ nm) with limited solubility (<10 mg/mL) in MQ water (Supporting Information Fig. S11).

Given the facts that ICP-2 showed a good balance between high solution iodine concentration and low viscosity, long term thermodynamic stability, and unimodal distribution with narrow dispersity in MQ water, DOTA-ICP (Table 1) was synthesized by using DOTA-CTA and following the RAFT copolymerization protocol of ICP-2 (Scheme 1B and Supporting Information Fig. S12). The 64 Cu radiolabeling result with specific activity of 0.037 MBq/µg polymer supported the successful introduction of DOTA that served as chelator for 64 Cu towards PET/CT dual-modality imaging. Interestingly, although the THF-SEC of DOTA-ICP (Fig. S12A) indicated its $M_{\rm n,\ THF-SEC}$ should be smaller than ICP-2, the measured value (67.0 kDa) was ca. 48% larger than the $M_{\rm n,\ THF-SEC}$ of ICP-2 (45.2 kDa), which was significantly different from the DMF-SEC (Table S1) and the DMF-DLS (Fig. 3) characterizations. The DOTA-ICP showed

similar DSC profile (Fig. S12B) as ICP-2, suggesting an effective "delocalization" of TIBEAs that was further validated through its high water solubility of >600 mg polymer/mL H₂O. As depicted in Fig. 3, the $R_{\rm h,\ water}$ of DOTA-ICP-fabricated NPs was close to the NPs from ICP-2. It is noteworthy that the R_h s of DOTA-ICP in THF and chloroform (CHCl₃) were different from other ICPs, which indicated the formation of nanoscopic assemblies in these two organic solvents. This observation also solved the $M_{\rm n.\ THF-SEC}$ variation issue (vide supra) as the obtained in-line refractive index increment (dn/dc) value in THF was not solely from DOTA-ICP single chains. The X-ray attenuation of the DOTA-ICP NPs was evaluated by acquiring images of a series of DOTA-ICP solutions with increased concentrations and subsequently converting them to Hounsfield Units (HU) for quantitative analysis. A linear correlation between DOTA-ICP concentration and the calculated CT attenuation was observed (Supporting Information Fig. S13), demonstrating that ICPs can function as contrast agents for quantitative CT studies.

The *in vivo* pharmacokinetics and metabolism/clearance of DOTA-ICP nano-XRCM after dilution to 0.9% saline with ⁶⁴Cu radiolabeling were evaluated through biodistribution studies (Fig. 4 and Supporting Information Tables S2—S4). As a proof-of-concept, BALB/c nude mice bearing EMT6 breast cancer tumor with significantly-developed vasculature were used (Supporting Information Fig. S14). The ⁶⁴Cu-DOTA-ICP NPs exhibited high initial blood retention, relatively-low hepatic and splenic accumulations, moderate renal clearance and significant tumor uptake at 1 h post-injection (p.i.). Significantly-prolonged blood circulation time of ⁶⁴Cu-DOTA-ICP NPs was confirmed by their gradually decreased blood retentions up to 72 h p.i.

 $(4.8 \pm 0.9\% \text{ ID/g})$ (Fig. 4A and Table S2). The liver and spleen uptakes showed similar trend with slightly increased accumulation at 24 h p.i., followed by constant retention for the next 48 h. The renal clearance indicated by kidney uptake demonstrated gradual excretion during the entire study, reasonably due to the portions of NPs with $R_h < 3$ nm, in combination with potential flexibility and dynamics of the polymers and their nanoassemblies. Metabolism studies revealed that most of the ⁶⁴Cu-DOTA-ICP NPs were excreted through feces with approximately 10% ID cleared from the renal system (Fig. 4B and Table S4). The tumor accumulations of ⁶⁴Cu-DOTA-ICP nano-XRCMs showed rapid increase from 1 h to 24 h p.i. and the accumulation remained stable (~20% ID/g) up to 72 h. The tumor-tomuscle (T/M) uptake ratios (Fig. 4C) revealed a similar pattern with ca. 2-fold increase determined at 24 h, followed by a constant value of ~ 10 throughout the study. The extended blood circulation and the persistent tumor retention provide robust foundations for application of ICP-based nano-XRCM as a dual-modality agent to monitor tumor progression while also having potential as treatment delivery vehicles.

PET/CT (Fig. 5A) and CT (Fig. 5B) imaging using ⁶⁴Cu-DOTA-ICP nano-XRCM in EMT6 tumors showed similar patterns as in the biodistribution studies. The selection of ⁶⁴Cu was attributed to its desirable nuclear properties ($t_{1/2} = 12.7 \text{ h}, \beta^+ = 17\%, \beta^- = 40\%$) for both imaging and potentially radionuclide therapy, as well as the suitable spatial resolution³³. High blood retention was determined in the heart and descending aorta during the first 4 h p.i. and then gradually decreased. Due to the ultrasmall size, renal clearance was also observed at 1 h (Fig. 5A, leftmost panel). The PET image at 1 h p.i. revealed low ⁶⁴Cu-DOTA-ICP uptake within tumor (standardized uptake value, SUV = 1.18 ± 0.16 , n = 8, Fig. 5C and Supporting Information Table S5) while little signals were visualized by CT imaging (Fig. 5B, leftmost panel). At 4 h p.i., the PET uptake slightly increased to SUV = 1.63 ± 0.22 (n = 8) with increased contrast observed in the corresponding CT image. Due to the extended blood residence, strong tumor uptake was determined by PET at 24 h with tripled uptake. Tumor accumulation reached the highest at 48 h, then slightly decreased at 72 h p.i. The T/M uptake ratios showed a comparable pattern to those acquired in biodistribution studies (Fig. 5D). Initial ratios were ~ 7 and then increased to 11.5 ± 0.78 (n = 8) at 24 h and remained constant until 72 h p.i. Importantly, in comparison with tumor uptake (SUV = 0.70 ± 0.13 , n = 6) and T/M ratios (3.25 ± 0.92 , n = 6) obtained with ¹⁸F-FDG (Supporting Information Table S6 and Fig. S15), the ⁶⁴Cu-DOTA-ICP NP demonstrated its advantage in

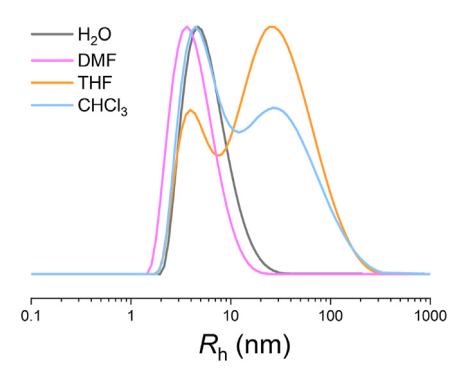


Figure 3 Intensity-weighted hydrodynamic radius distributions of DOTA-ICP in H₂O, DMF, THF, and CHCl₃, respectively, determined *via* DLS with concentration of DOTA-ICP at 10 mg/mL.

tumor uptake and T/M contrast. Consistent with PET, CT images demonstrated the increased accumulation of 64 Cu-DOTA-ICP nano-XRCM in tumor over time until 48 h, as confirmed by the continuous increase of CT tumor contrast (Supporting Information Table S7) and the longitudinally-clear tumor visualizations (Fig. 5B). At 72 h p.i., the sufficient blood retention ($6.60 \pm 1.11\%$ ID) and the slow tumor excretion of DOTA-ICP nano-XRCM, as well as the clearance from other organs except liver (Table S3), ensured higher CT contrast of tumor architecture (Fig. 5B, rightmost panel).

3. Discussion

The ICP-based ultrasmall nano-XRCM showed high aqueous iodine concentration, low solution viscosity, long-term thermodynamic stability, and DP_n-independent intensity-weighted hydrodynamic radii of ca. 5 nm. In vivo biodistribution evaluation of ⁶⁴Cu-DOTA-ICP nano-XRCM revealed its prolonged blood circulation, low nonspecific organ accumulations, high tumor uptake and retention, as well as effective clearance (ca. 46% within 48 h p.i.) through the hepatic and renal pathways. These optimal physicochemical and in vivo pharmacokinetic characteristics enabled practical PET/CT dual-modality tumor imaging within significantly-extended operation time windows after single intravenous administration. The tumor identification and quantification were realized through highly-sensitive and functional PET up to 72 h p.i., while convenient tumor monitoring was granted by dynamic and longitudinal CT up to 10 day p.i. (Fig. 6). Quantitative analyses of both imaging modalities showed sufficient correlation (Fig. 5E). Clear visualizations of tumor, including the tumor heterogeneities, without noticeable interferences from other organs were achieved and maintained after 24 h p.i., which suggested that accumulation of DOTA-ICP nano-XRCM in tumor proceeded through the enhanced permeability and retention effect⁴⁹. The administered dose, $\sim 1.8 \mu g$ iodine/g (calculated based upon 35.8 wt% of iodine content, 100 μg iodine/mouse, and ca. 20 g of mouse body weight), was substantially low for attaining tumor differential CT contrast (>200 HU at 72 h p.i.) by using the conventional CT scanner of a micro-PET/CT combo instrument, which avoids the need for advanced micro-CT instrumental features. The sub-10 mg iodine/kg dose, together with the low viscosity and osmolality of ICP nano-XRCM at ~140 mg iodine/mL H₂O concentration, also ensured small injection volumes of contrast agent solution and low kidney burden, in contrast to typical agents associated with contrast-enhanced CT imaging.

Due to the moderate half-life of ⁶⁴Cu (12.7 h), PET imaging with ⁶⁴Cu-DOTA-ICP nano-XRCM over 72 h p.i. was less reliable. This could be practically improved through introducing desferrioxamine (DFO), a chelator for ⁸⁹Zr PET isotope with half-life of 78.4 h, to ICP system by utilizing DFO-CTA during the RAFT copolymerization process. It should be noted, although ⁸⁹Zr-DFO-ICP nano-XRCM might enable the longitudinal tumor monitoring by PET and CT dual imaging modalities within comparable time frame, the PET imaging quality could be compromised by the much higher positon range of ⁸⁹Zr *in vivo* compared to ¹⁸F and ⁶⁴Cu PET isotopes⁵⁰.

4. Conclusions

In conclusion, a facile and convenient strategy was developed for the preparation of ultrasmall iodinated nanoparticles capable of contrast-enhanced CT imaging. As previously reported^{43–46} and

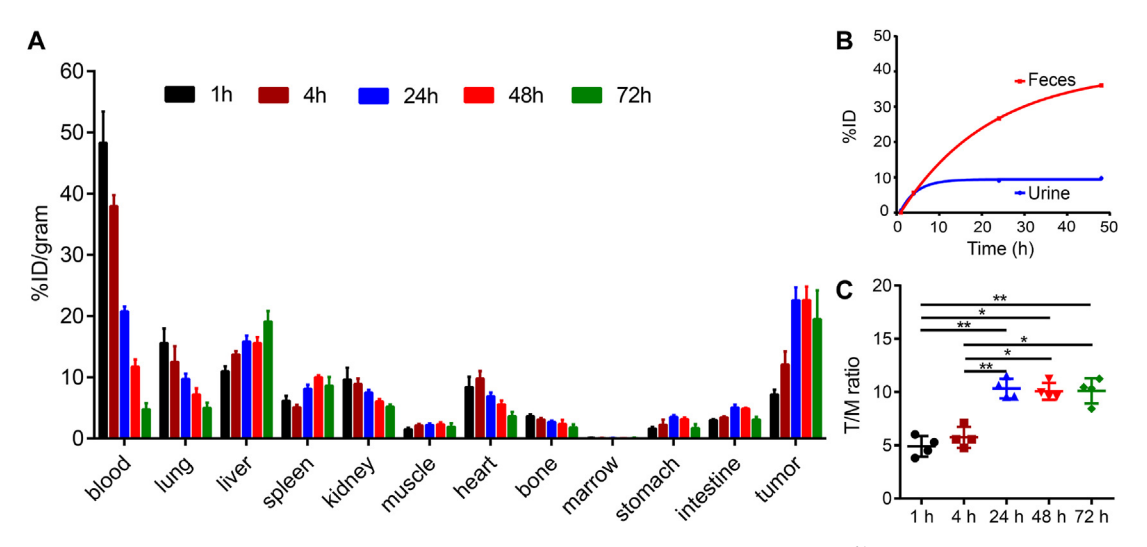


Figure 4 Biodistribution (A), clearance (B), and tumor-to-muscle (T/M) uptake ratio (C) profiles of 64 Cu-DOTA-ICP nano-XRCM in BALB/c nude mice bearing EMT6 breast cancer tumor at 1, 4, 24, 48, and 72 h post intravenous injection *via* tail vein, respectively (0.185 MBq/mice injection, \sim 5.0 µg polymer/mice, n = 4/group). *P < 0.05, **P < 0.01.

further elaborated by the ICPs presented in this work, the ultrasmall sizes of nanostructures obtained through aqueous cross-backbone assembly of amphiphilic statistical copolymers may be independent of structural variations of polymer precursors. A simple process of intra/intermolecular self-assembly of DOTA-

ICPs in aqueous solution afforded nanoscopic imaging agents that are active as both nano-XRCM and PET tracers, which showed high iodine concentration, good biocompatibility, long blood circulation time, significant accumulation in tumor, and slow tumor excretion for noninvasive PET/CT imaging-based

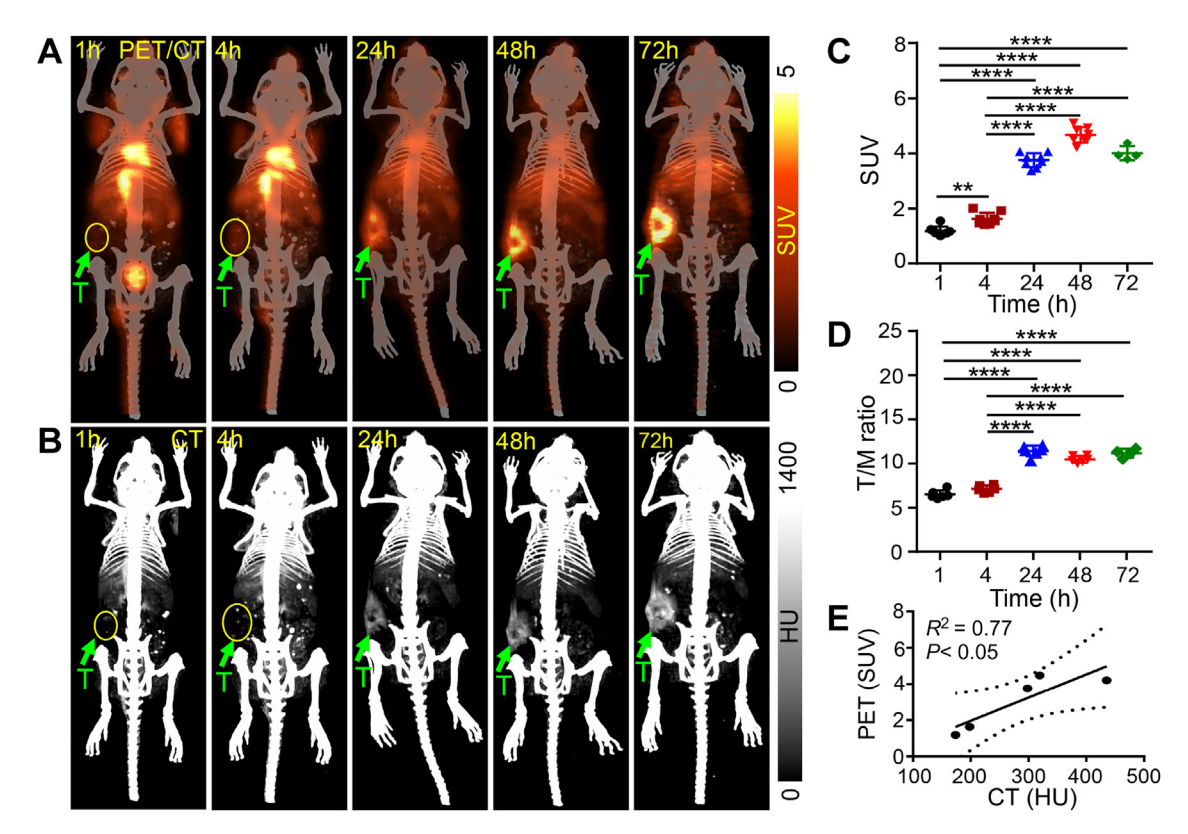


Figure 5 Representative PET/CT (A) and CT (B) transverse images, PET SUVs within tumor (C), PET T/M contrast ratios (D), and PET-CT correlation (E) of BABL/c nude mice bearing EMT6 breast cancer tumor after intravenous injection of 64 Cu-DOTA-ICP nano-XRCM *via* tail vein (3.7 MBq/mice injection, ~100 µg polymer/mice, ~1.8 µg iodine/g mice body weight) at 1, 4, 24, 48 h (n = 8/group), and 72 h (n = 4/group) post-injection, respectively. The tumor region is indicated by the green arrow and/or yellow circle. ****P < 0.001.

dynamic and longitudinal tumor monitoring after a single administration. Their potential applications in multi-modality imaging-based diagnosis and -guided therapy of cancers over long time durations were highlighted. Comprehensive *in vivo* toxicity evaluations, future optimizations and developments are underway, including enhancing renal clearance, introducing tumor biomarker targeting capability, and advancing into theranostic scaffolds. The relatively straightforward synthetic approach and direct supramolecular assembly process makes this nano-XRCM system easily transferrable across laboratories to facilitate direct and broad translation potential.

5. Experimental

5.1. EMT6 mouse breast cancer model

Murine EMT6 mammary carcinoma cells were cultured in Waymouth's MB 752/1 medium with 85% of 2 mmol/L L-glutamine and 15% of fetal bovine serum at 37 °C with 5% CO₂. BALB/c nude mice (Charles River Laboratory, Wilmington, MA) weighing approximately 25 g were subcutaneously implanted with 6×10^5 EMT6 cells into the right flank. The tumors were allowed to grow for 10 days (tumor approximately 0.3–0.4 g) prior to biodistribution and PET imaging.

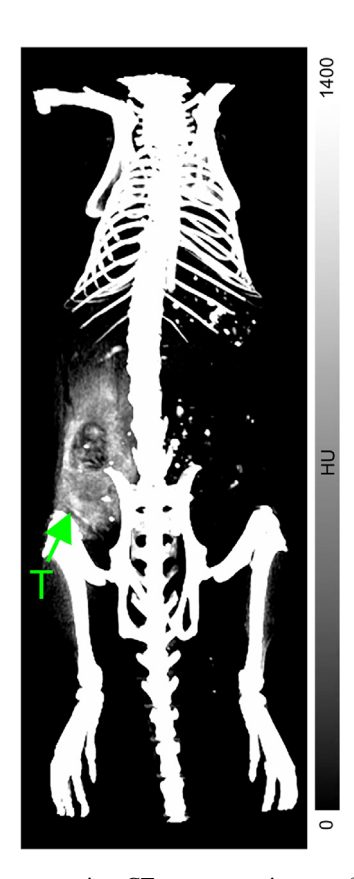


Figure 6 Representative CT transverse image of BABL/c nude mice bearing EMT6 breast cancer tumor after intravenous injection of 64 Cu-DOTA-ICP nano-XRCM *via* tail vein (3.7 MBq/mice injection, $\sim 100 \mu g$ polymer/mice, $\sim 1.8 \mu g$ iodine/g mice body weight) at 10 day (n = 4/group) post-injection. The tumor region is indicated by the green arrow.

5.2. ⁶⁴Cu radiolabeling

 64 Cu was produced on the Washington University Medical School CS-15 cyclotron by the 64 Ni (p,n) 64 Cu nuclear reaction at a specific activity of 1.85–7.4 GBq/mg at the end of bombardment. DOTA-ICP (~4.5 μg) were incubated with 18.5 MBq of 64 Cu in 100 μL of 0.1 mol/L pH 5.5 ammonium acetate buffer at 45 °C for 1 h (n=3). After ethylenediamine tetraacetic acid (EDTA) challenge (10 mmol/L in 50 mmol/L, pH 7.4, phosphate buffer), the radiochemical purities of the radiolabeled nanoparticles were measured by radioactive thin-layer chromatography (Bioscan, Washington, DC), followed by the purification with 7k Zeba spin desalting column (Piercenet, Rockford, IL). 64 Cu radiolabeling yields: > 95%. Radiochemical purities: > 99%.

5.3. Serum stability study

The radiochemical purities of 64 Cu radiolabeled DOTA-ICP was measured before the addition of mouse serum with 1:1 volume ratio. The 64 Cu-DOTA-ICP and serum mixture was incubated in microcentrifuge tubes at 45 °C. At each time point (1, 4, 24 and 48 h postinjection), 10 μ L of the sample was removed and incubated at 45 °C with 5 μ L of EDTA (10 mmol/L in 50 mmol/L pH 7.4 phosphate buffer) for 5 min. The radiochemical purities of the samples (n=3) were tested using radioactive thin-layer chromatography (Bioscan, Washington, DC). Radiochemical purities: >95%.

5.4. Ex vivo biodistribution study

All animal studies were performed in compliance with guidelines set forth by the NIH Office of Laboratory Animal Welfare and approved by the Washington University Animal Studies Committee. *In vivo* biodistribution studies were performed using 185 kBq of 64 Cu-DOTA-ICP (5 µg polymer/mice) in 100 µL saline (APP Pharmaceuticals, Schaumburg, IL) injected *via* the tail vein of EMT6 tumor bearing mice weighing 20-25 g (n=4/group) under inhaled isoflurane. The mice were euthanized by cervical dislocation at each time point (1, 4, 24, 48, and 72 h post-injection). Organs of interest were collected, weighed, and counted in a well gamma counter (Beckman 8000). Standards were prepared and measured along with the organs to calculate the average and standard deviation of the percentage of the injected dose per gram of tissue (% ID/g).

5.5. In vivo CT and PET/CT studies

Ten days after the EMT6 murine mammary carcinoma cells implantation, mice were anesthetized with isoflurane and injected with 3.7 MBq of ⁶⁴Cu-DOTA-ICP in 100 μL of saline *via* the tail vein. PET scans were performed on either microPET Focus 220 (Siemens, Malvern, PA) or Inveon PET/CT system (Siemens, Malvern, PA) at 1, 4, 24, 48, and 72 h post-injection. ¹⁸F-FDG PET was also performed at 1 h post injection of 7.4 MBq ¹⁸F-FDG in saline via tail vein. The PET images were corrected for attenuation, scatter, normalization, and camera dead time and coregistered with CT images. All of the PET scanners were crosscalibrated periodically. The PET images were reconstructed with the maximum a posteriori (MAP) algorithm and analyzed by Inveon Research Workplace. The tumor uptake of ⁶⁴Cu-DOTA-ICP and ¹⁸F-FDG was calculated as percent injected dose per gram of tissue (% ID/g) in three-dimensional regions of interest (ROIs). All PET data were not corrected for partial volume effect.

5.6. RAFT copolymerizations to afford ICPs

5.6.1. ICP-1

To a 50 mL Schlenk flask equipped with a magnetic stirring bar dried with flame under N2 atmosphere, was added 2-(dodecylthiocarbonothioylthio)-2-methyl propanoic acid (DDMAT, 32.2 mg, 88.0 μmol), TIBEA (2.6 g, 4.4 mmol), OEGMEA (2.1 g, 4.4 mmol), 2,2'-azobisisobutyronitrile (AIBN, 2.2 mg, 13 μmol), 2 mL of DMF, and 16 mL of 1,4-dioxane. The mixture was stirred 10 min at rt, deoxygenated through four cycles of freeze-pump-thaw, and back-filled with N₂. After the last cycle, the reaction mixture was stirred 10 min at rt and immersed into a pre-heated oil bath at 63 °C to start the polymerization. The polymerization was quenched after 9 h by cooling the reaction flask with liquid N2. The resulting mixture was diluted with 10 mL of CH₂Cl₂ and precipitated into 250 mL of diethyl ether. Centrifugation-collected precipitates were dissolved in 20 mL of CH₂Cl₂ and precipitated into 180 mL of diethyl ether. The precipitates were collected through centrifugation and kept under vacuum overnight to remove residual solvents, yielding a yellow oil (71% yield based upon comonomer conversions). $M_{\rm n, THF\text{-}SEC} = 28.2 \,\text{kDa}, D = 1.2. \,M_{\rm n, DMF\text{-}SEC} = 16.7 \,\text{kDa},$ D = 1.3. ¹H NMR (500 MHz, CD₂Cl₂, ppm) δ 8.31 (br), 7.79 (br), 4.48 (br), 4.35 (br), 4.14 (br), 3.57 (s), 3.49 (br), 3.32 (br), 2.55-0.98 (m), 0.86 (t, J = 6.8 Hz). ¹³C NMR (126 MHz, CDCl₃, ppm) δ , 221.07, 174.04, 165.43, 148.77, 140.90, 137.13, 113.56, 107.00, 93.95, 71.87, 70.49, 68.77, 63.94, 63.49, 62.06, 59.00, 41.16, 34.96, 31.87, 29.59, 22.65, 14.12. FT-IR (ATR): 3755-3230, 2859, 1730, 1544, 1521, 1449, 1393, 1350, 1268, 1097, 1001, 947, 852 cm⁻¹. $T_{\rm g} = -33 \, {\rm ^{\circ}C}$. TGA in Ar, 290–423 ${\rm ^{\circ}C}$, 91% mass loss.

5.6.2. ICP-2

To a 50 mL Schlenk flask equipped with a magnetic stirring bar dried with flame under N₂ atmosphere, was added DDMAT (73.6 mg, 0.2 mmol), TIBEA (6.0 g, 10 mmol), OEGMEA (4.8 g, 10 mmol), AIBN (3.3 mg, 20 µmol), and 24 mL of 1,4-dioxane. The mixture was stirred 10 min at rt, deoxygenated through four cycles of freeze-pump-thaw, and back-filled with N2. After the last cycle, the reaction mixture was stirred 10 min at rt and immersed into a preheated oil bath at 62 °C to start the polymerization. The polymerization was quenched after 12 h by cooling the reaction flask with liquid N₂. The resulting mixture was diluted with 10 mL of CH₂Cl₂ and precipitated into 300 mL of diethyl ether. Centrifugationcollected precipitates were dissolved in 20 mL of CH₂Cl₂ and precipitated into 180 mL of diethyl ether. The precipitates were collected through centrifugation and kept under vacuum overnight to remove residual solvents, yielding a yellow oil (89% yield based upon comonomer conversions). $M_{\rm n, THF-SEC} = 45.2 \, \rm kDa$, D = 1.2. $M_{\rm n, \, DMF-SEC} = 25.5 \, \rm kDa$, D = 1.3. The ¹H NMR, ¹³C NMR, and FT-IR were similar as ICP-1. $T_{\rm g} = -32$ °C. TGA in Ar, 295–434 °C (93% mass loss).

5.6.3. ICP-3

To a 50 mL Schlenk flask equipped with a magnetic stirring bar dried with flame under N_2 atmosphere, was added DDMAT (24.1 mg, 65.9 µmol), TIBEA (5.9 g, 9.9 mmol), OEGMEA (4.8 g, 9.9 mmol), AIBN (1.8 mg, 11 µmol), and 16 mL of 1,4-dioxane. The mixture was stirred 10 min at rt, deoxygenated through four cycles of freeze—pump—thaw, and back-filled with N_2 . After the last cycle, the reaction mixture was stirred 10 min at rt and immersed into a pre-heated oil bath at 62 °C to start the polymerization. The polymerization was quenched after 33.5 h by cooling the reaction flask with liquid N_2 . The resulting mixture

was diluted with 10 mL of CH₂Cl₂ and precipitated into 300 mL of diethyl ether. Centrifugation-collected precipitates were dissolved in 20 mL of THF and precipitated into 180 mL of diethyl ether. The precipitates were collected through centrifugation and kept under vacuum overnight to remove residual solvents, yielding a yellow oil (78% yield based upon comonomer conversions). $M_{\rm n, THF-SEC} = 138.5$ kDa, D = 1.4. $M_{\rm n, DMF-SEC} = 53.4$ kDa, D = 1.6. The ¹H NMR, ¹³C NMR, and FT-IR were similar as ICP-1. $T_{\rm g} = -35$ °C. TGA in Ar, 300–438 °C (94% mass loss).

5.7. RAFT copolymerization to afford DOTA-ICP (ICP-4)

To a 50 mL Schlenk flask equipped with a magnetic stirring bar dried with flame under N₂ atmosphere, was added DOTA-CTA (74.0 mg, 93.3 µmol), TIBEA (2.8 g, 4.7 mmol), OEGMEA (2.3 g, 4.7 mmol), AIBN (1.5 mg, 9.4 µmol), 5 mL of DMF, and 7 mL of 1,4-dioxane. The mixture was stirred 10 min at rt, deoxygenated through five cycles of freeze-pump-thaw, and back-filled with N_2 . After the last cycle, the reaction mixture was stirred 10 min at rt and immersed into a pre-heated oil bath at 65 °C to start the polymerization. The polymerization was quenched after 16.5 h by cooling the reaction flask with liquid N2. The resulting mixture was precipitated into 130 mL of diethyl ether. Centrifugation-collected precipitates were dissolved in 12 mL of CH₂Cl₂ and precipitated into 130 mL of diethyl ether. The precipitates were collected through centrifugation and kept under vacuum overnight to remove residual solvents, yielding a yellow oil (87% yield based upon comonomer conversions). $M_{\text{n, THF-SEC}} = 67.0 \,\text{kDa}$, $D = 1.3 \,M_{\text{n, DMF-SEC}} = 22.7 \,\text{kDa}$, D = 1.5. ¹H NMR (500 MHz, CD₂Cl₂, ppm) δ 8.31 (br), 7.79 (br), 4.48 (br), 4.35 (br), 4.14 (br), 3.57 (s), 3.49 (br), 3.32 (br), 2.55–0.98 (m), 0.86 (t, J = 6.8 Hz). ¹³C NMR (126 MHz, CDCl₃, ppm) δ , 221.07, 174.04, 165.43, 148.77, 140.90, 137.13, 113.56, 107.00, 93.95, 71.87, 70.49, 68.77, 63.94, 63.49, 62.06, 59.00, 41.16, 34.96, 31.87, 29.59, 22.65, 14.12. FT-IR (ATR): 3755-3230, 2859, 1730, 1544, 1521, 1449, 1393, 1350, 1268, 1097, 1001, 947, 852 cm⁻¹. $T_{\rm g} = -33 \, {\rm ^{\circ}C}$. TGA in Ar, 290–423 ${\rm ^{\circ}C}$, 91% mass loss.

Acknowledgments

We gratefully acknowledge financial support from the National Science Foundation (DMR-1905818 and REU Grant CHE-1062840, USA) and the Robert A. Welch Foundation through the W. T. Doherty-Welch Chair in Chemistry (A-0001, USA). The Laboratory for Synthetic-Biologic Interactions (LSBI) at Texas A&M University (College Station, TX, USA) is also acknowledged. We thank Prof. Chong Cheng and Dr. Yukun Li (University at Buffalo, The State University of New York, Buffalo, NY, USA) for assisting with DMF-SEC characterizations, Prof. Ilja Voets and Lafayette de Windt (Eindhoven University of Technology, Eindhoven, The Netherlands) for discussion of SLS/DLS results.

Author contributions

Guorong Sun, Yongjian Liu, and Karen L. Wooley designed research. Lu Su, Kellie S. Dalby, Hannah Luehmann, Sussana A. Elkassih, Sangho Cho, Xun He, Lisa Detering, Yen-Nan Lin, Nari Kang, Dennis A. Moore, Richard Laforest, and Guorong Sun performed research. Lu Su, Kellie S. Dalby, Hannah Luehmann, Guorong Sun, Yongjian Liu, and Karen L. Wooley analyzed data. Lu Su, Kellie S. Dalby, Guorong Sun, Yongjian Liu, and Karen L. Wooley wrote the paper.

Conflicts of interest

The authors have no conflicts of interest to declare.

Appendix A. Supporting information

Supporting data to this article can be found online at https://doi.org/10.1016/j.apsb.2022.09.009.

References

- Rubin GD. Computed Tomography: revolutionizing the practice of medicine for 40 years. *Radiology* 2014;273:S45-74.
- de Vries EGE, Kist de Ruijter L, Lub-de Hooge MN, Dierckx RA, Elias SG, Oosting SF. Integrating molecular nuclear imaging in clinical research to improve anticancer therapy. *Nat Rev Clin Oncol* 2019; 16:241–55.
- 3. Lusic H, Grinstaff MW. X-ray-computed tomography contrast agents. *Chem Rev* 2013;**113**:1641–66.
- Koç MM, Aslan N, Kao AP, Barber AH. Evaluation of X-ray tomography contrast agents: a review of production, protocols, and biological applications. *Microsc Res Tech* 2019;82:812

 –48.
- Schöckel L, Jost G, Seidensticker P, Lengsfeld P, Palkowitsch P, Pietsch H. Developments in X-Ray contrast media and the potential impact on computed tomography. *Invest Radiol* 2020;55:592-7.
- Jakhmola A, Anton N, Vandamme TF. Inorganic nanoparticles based contrast agents for X-ray computed tomography. Adv Healthc Mater 2012;1:413

 –31
- Aslan N, Ceylan B, Koç MM, Findik F. Metallic nanoparticles as X-Ray computed tomography (CT) contrast agents: a review. J Mol Struct 2020;1219:128599.
- Ghaghada KB, Badea CT, Karumbaiah L, Fettig N, Bellamkonda RV, Johnson GA, et al. Evaluation of tumor microenvironment in an animal model using a nanoparticle contrast agent in computed tomography imaging. *Acad Radiol* 2011;18:20-30.
- Hyafil F, Cornily JC, Feig JE, Gordon R, Vucic E, Amirbekian V, et al. Noninvasive detection of macrophages using a nanoparticulate contrast agent for computed tomography. Nat Med 2007;13:636–41.
- Lim SJ, Lim JS, Choi J, Choi JY, Hyung WJ, Kim HS, et al. Nanoscaled iodized oil emulsion as a CT contrast agent for the detection of experimental liver tumors in a rat model. *Acad Radiol* 2010;17: 985–91.
- Trubetskoy VS, Gazelle GS, Wolf GL, Torchilin VP. Block-copolymer of polyethylene glycol and polylysine as a carrier of organic iodine: design of long-circulating particulate contrast medium for X-ray computed tomography. J Drug Target 1997;4:381–8.
- Torchilin VP, Frank-Kamenetsky MD, Wolf GL. CT visualization of blood pool in rats by using long-circulating, iodine-containing micelles. Acad Radiol 1999;6:61–5.
- Galperin A, Margel D, Baniel J, Dank G, Biton H, Margel S. Radiopaque iodinated polymeric nanoparticles for X-ray imaging applications. *Biomaterials* 2007;28:4461–8.
- Aviv H, Bartling S, Kieslling F, Margel S. Radiopaque iodinated copolymeric nanoparticles for X-ray imaging applications. *Bio-materials* 2009;30:5610-6.
- Yin Q, Yap FY, Yin L, Ma L, Zhou Q, Dobrucki LW, et al. Poly(iohexol) nanoparticles as contrast agents for *in vivo X-ray* computed tomography imaging. *J Am Chem Soc* 2013;135:13620–3.
- Jin E, Lu ZR. Biodegradable iodinated polydisulfides as contrast agents for CT angiography. *Biomaterials* 2014;35:5822-9.
- Zou Y, Wei Y, Wang G, Meng F, Gao M, Storm G, et al. Nanopolymersomes with an ultrahigh iodine content for high-performance X-Ray computed tomography imaging. in vivo. Adv Mater 2017;29: 1603997
- Wallyn J, Anton N, Serra CA, Bouquey M, Collot M, Anton H, et al. A new formulation of poly(MAOTIB) nanoparticles as an efficient

- contrast agent for *in vivo* X-ray imaging. *Acta Biomater* 2018;**66**: 200–12.
- Hainfeld JF, Ridwan SM, Stanishevskiy Y, Smilowitz NR, Davis J, Smilowitz HM. Small, long blood half-life iodine nanoparticle for vascular and tumor imaging. Sci Rep 2018;8:13803.
- Tian L, Lu L, Feng J, Melancon MP. Radiopaque nano and polymeric materials for atherosclerosis imaging, embolization and other catheterization procedures. Acta Pharm Sin B 2018;8:360-70.
- Duan X, Cao Z, Zhu H, Liu C, Zhang X, Zhang J, et al. ⁶⁸Ga-labeled ODAP-Urea-based PSMA agents in prostate cancer: first-in-human imaging of an optimized agent. *Eur J Nucl Med Mol Imag* 2022;49: 1030–40.
- Zhou H, Wang Y, Xu H, Shen X, Zhang T, Zhou X, et al. Noninvasive interrogation of CD8+ T cell effector function for monitoring tumor early responses to immunotherapy. J Clin Invest 2022;132:e161065.
- Hu K, Li J, Wang L, Huang Y, Li L, Ye S, et al. Preclinical evaluation and pilot clinical study of [¹⁸F]AlF-labeled FAPI-tracer for PET imaging of cancer associated fibroblasts. *Acta Pharm Sin B* 2022;12: 867-75.
- 24. Hu K, Wu W, Xie L, Geng H, Zhang Y, Hanyu M, et al. Whole-body PET tracking of a p-dodecapeptide and its radiotheranostic potential for PD-L1 overexpressing tumors. *Acta Pharm Sin B* 2022;12:1363–76.
- Farwell MD, Pryma DA, Mankoff DA. PET/CT imaging in cancer: current applications and future directions. Cancer 2014;120:3433—45.
- Furlow B. PET-CT cancer imaging. Radiol Technol 2018;90: 149CT-70CT.
- Zheng L, Zhu R, Chen L, Fu Q, Li J, Chen C, et al. X-ray sensitive high-Z metal nanocrystals for cancer imaging and therapy. *Nano Res* 2021;14:3744-55.
- Zarschler K, Rocks L, Licciardello N, Boselli L, Polo E, Garcia KP, et al. Ultrasmall inorganic nanoparticles: state-of-the-art and perspectives for biomedical applications. *Nanomed Nanotechnol Biol Med* 2016;12:1663-701.
- Jiang X, Du B, Huang Y, Zheng J. Ultrasmall noble metal nanoparticles: breakthroughs and biomedical implications. *Nano Today* 2018;21:106–25.
- Hainfeld JF, Slatkin DN, Focella TM, Smilowitz HM. Gold nanoparticles: a new X-ray contrast agent. Br J Radiol 2006;79:248-53.
- **31.** Tsvirkun D, Ben-Nun Y, Merquiol E, Zlotver I, Meir K, Weiss-Sadan T, et al. CT imaging of enzymatic activity in cancer using covalent probes reveal a size-dependent pattern. *J Am Chem Soc* 2018; **140**:12010–20.
- Luo D, Wang X, Zeng S, Ramamurthy G, Burda C, Basilion JP. Prostate-specific membrane antigen targeted gold nanoparticles for prostate cancer radiotherapy: does size matter for targeted particles?. *Chem Sci* 2019;10:8119–28.
- 33. Zhao Y, Detering L, Sultan D, Cooper ML, You M, Cho S, et al. Gold nanoclusters doped with ⁶⁴Cu for CXCR4 positron emission tomography imaging of breast cancer and metastasis. ACS Nano 2016;10: 5959-70.
- Kreyling WG, Abdelmonem AM, Ali Z, Alves F, Geiser M, Haberl N, et al. *In vivo* integrity of polymer-coated gold nanoparticles. *Nat Nanotechnol* 2015;10:619–23.
- Huang YW, Wu CH, Aronstam RS. Toxicity of transition metal oxide nanoparticles: recent insights from *in vitro* studies. *Materials* 2010;3: 4842–59.
- Yao Y, Zang Y, Qu J, Tang M, Zhang T. The toxicity of metallic nanoparticles on liver: the subcellular damages, mechanisms, and outcomes. *Int J Nanomed* 2019;14:8787–804.
- IdÉE J-M, Port M, Robert P, Raynal I, Prigent P, Dencausse A, et al. Preclinical profile of the monodisperse iodinated macromolecular blood pool agent P743. *Invest Radiol* 2001;36:41–9.
- You S, Jung HY, Lee C, Choe YH, Heo JY, Gang GT, et al. Highperformance dendritic contrast agents for X-ray computed tomography imaging using potent tetraiodobenzene derivatives. *J Control Release* 2016;226:258–67.
- Gaikwad HK, Tsvirkun D, Ben-Nun Y, Merquiol E, Popovtzer R, Blum G. Molecular imaging of cancer using X-ray computed

tomography with protease targeted iodinated activity-based probes. *Nano Lett* 2018;**18**:1582–91.

- Corrigan N, Jung K, Moad G, Hawker CJ, Matyjaszewski K, Boyer C. Reversible-deactivation radical polymerization (controlled/living radical polymerization): from discovery to materials design and applications. *Prog Polym Sci* 2020;111:101311.
- Yu W, Maynard E, Chiaradia V, Arno MC, Dove AP. Aliphatic polycarbonates from cyclic carbonate monomers and their application as biomaterials. *Chem Rev* 2021;121:10865—907.
- Yin L, Cheng J, Deming TJ, Vicent MJ. Synthetic polypeptides for drug and gene delivery, and tissue engineering. Adv Drug Deliv Rev 2021;178:113995.
- Hirai Y, Terashima T, Takenaka M, Sawamoto M. Precision selfassembly of amphiphilic random copolymers into uniform and self-sorting nanocompartments in water. *Macromolecules* 2016;49: 5084-91.
- Imai S, Hirai Y, Nagao C, Sawamoto M, Terashima T. Programmed self-assembly systems of amphiphilic random copolymers into sizecontrolled and thermoresponsive micelles in water. *Macromolecules* 2018;51:398–409.

- 45. Hattori G, Hirai Y, Sawamoto M, Terashima T. Self-assembly of PEG/dodecyl-graft amphiphilic copolymers in water: consequences of the monomer sequence and chain flexibility on uniform micelles. *Polym Chem* 2017;8:7248–59.
- 46. Hattori G, Takenaka M, Sawamoto M, Terashima T. Nanostructured materials via the pendant self-assembly of amphiphilic crystalline random copolymers. J Am Chem Soc 2018;140:8376—9.
- Perrier S. 50th Anniversary perspective: RAFT polymerization—a user guide. *Macromolecules* 2017;50:7433–47.
- **48.** Lutz JF. Polymerization of oligo(ethylene glycol) (meth)acrylates: toward new generations of smart biocompatible materials. *J Polym Sci: Polym Chem* 2008;**46**:3459–70.
- **49.** Zhang M, Gao S, Yang D, Fang Y, Lin X, Jin X, et al. Influencing factors and strategies of enhancing nanoparticles into tumors *in vivo*. *Acta Pharm Sin B* 2021;**11**:2265–85.
- Carter LM, Kesner AL, Pratt EC, Sanders VA, Massicano AVF, Cutler CS, et al. The impact of positron range on PET resolution, evaluated with phantoms and PHITS Monte Carlo simulations for conventional and non-conventional radionuclides. *Mol Imag Biol* 2019;22:73—84.